

## EUV spectroscopy of highly charged $\text{Sn}^{13+}$ – $\text{Sn}^{15+}$ ions in an electron-beam ion trap

J. Scheers<sup>1,2</sup>, C. Shah<sup>3</sup>, A. Ryabtsev<sup>4</sup>, H. Bekker<sup>3</sup>, F. Torretti<sup>1,2</sup>, J. Sheil<sup>1</sup>, D. A. Czapski<sup>5</sup>, J. C. Berengut<sup>5</sup>,  
W. Ubachs<sup>1,2</sup>, J. R. Crespo López-Urrutia<sup>3</sup>, R. Hoekstra<sup>1,6</sup>, and O. O. Versolato<sup>1,\*</sup>

<sup>1</sup>Advanced Research Center for Nanolithography, Science Park 110, 1098 XG Amsterdam, Netherlands

<sup>2</sup>Department of Physics and Astronomy, and LaserLaB, Vrije Universiteit, De Boelelaan 1081, 1081 HV Amsterdam, Netherlands

<sup>3</sup>Max-Planck-Institut für Kernphysik, Saupfercheckweg 1, 69117 Heidelberg, Germany

<sup>4</sup>Institute of Spectroscopy, Russian Academy of Sciences, Troitsk, Moscow 108840, Russia

<sup>5</sup>School of Physics, University of New South Wales, Sydney 2052, Australia

<sup>6</sup>Zernike Institute for Advanced Materials, University of Groningen, Nijenborgh 4, 9747 AG Groningen, Netherlands



(Received 7 November 2019; accepted 13 May 2020; published 15 June 2020)

Extreme-ultraviolet (EUV) spectra of  $\text{Sn}^{13+}$ – $\text{Sn}^{15+}$  ions have been measured in an electron-beam ion trap (EBIT). A matrix inversion method is employed to unravel convoluted spectra from a mixture of charge states typically present in an EBIT. The method is benchmarked against the spectral features of resonance transitions in  $\text{Sn}^{13+}$  and  $\text{Sn}^{14+}$  ions. Three new EUV lines in  $\text{Sn}^{14+}$  confirm its previously established level structure. This ion is relevant for EUV nanolithography plasma but no detailed experimental data currently exist. We used the Cowan code for first line identifications and assignments in  $\text{Sn}^{15+}$ . The collisional-radiative modeling capabilities of the Flexible Atomic Code were used to include line intensities in the identification process. Using the 20 lines identified, we have established 17 level energies of the  $4p^44d$  configuration as well as the fine-structure splitting of the  $4p^5$  ground-state configuration. Moreover, we provide state-of-the-art *ab initio* level structure calculations of  $\text{Sn}^{15+}$  using the configuration-interaction many-body perturbation code AMBiT. We find that the here-dominant emission features from the  $\text{Sn}^{15+}$  ion lie in the narrow 2% bandwidth around 13.5 nm that is relevant for plasma light sources for state-of-the-art nanolithography.

DOI: [10.1103/PhysRevA.101.062511](https://doi.org/10.1103/PhysRevA.101.062511)

### I. INTRODUCTION

Extreme-ultraviolet (EUV) light emission near 13.5 nm wavelength from highly charged tin ions, primarily from  $4p$ – $4d$  and  $4d$ – $4f$  transitions in  $\text{Sn}^{8+}$ – $\text{Sn}^{14+}$ , is the source of light for state-of-the-art nanolithography [1–5]. Accurate knowledge of the open  $4d$ -subshell atomic structure of these ions provides insight for further optimization of EUV light emission of industrial laser-driven plasma sources. The electronic structure of the involved tin ions is extremely complicated, in part due to the existence of strong configuration-interaction effects. Spectroscopic accuracy remains inaccessible to even the most advanced atomic codes. Given their importance, the spectra of these charge states have been widely investigated [6–14]. Recently, however, evidence was found calling for a revision of earlier identifications of transitions in  $\text{Sn}^{8+}$ – $\text{Sn}^{14+}$  ions [15,16]. Furthermore, no experimental atomic structure data are available on the neighboring charge state  $\text{Sn}^{15+}$ , with its open  $4p$ -subshell  $4p^5$  ground-state configuration. Emission from tin ions in charge

state  $15+$  is however readily observed from the relatively weak  $4p$ – $5s$  transitions near 7 nm in EUV-generating laser-produced tin plasmas [17,18]. Understanding the contribution of the stronger  $4p$ – $4d$  transitions of  $\text{Sn}^{15+}$  (as compared to its  $4p$ – $5s$  transitions) to the industrially relevant emission feature at 13.5 nm should therefore be particularly relevant for simulations of such plasmas. New experimental tin data are thus required.

Experimental investigations are hampered by the fact that plasmas, including plasma in electron-beam ion traps (EBITs) [19–24], that are typically required to produce ions in intermediate charge states, contain a mixture of ions of different charge states with overlapping spectral features. Charge-state-resolved spectra can be obtained using suitable subtractions of spectra acquired under various plasma conditions [25–28] or by employing genetic algorithms [29]. In this work, we employ a matrix inversion method to obtain charge-state-resolved spectra using matrix inversion techniques on convoluted, mixed-charge-state EUV spectra experimentally obtained from an electron-beam ion trap.

We focus here on the EUV spectra of  $\text{Sn}^{13+}$ – $\text{Sn}^{15+}$ . Their strongest line features are particularly closely spaced and offer a rather tractable atomic structure with a relatively limited number of strong transitions. First, as a benchmark, we use the matrix inversion method to reevaluate the  $4p^64d$ – $(4p^54d^2 + 4p^64f + 4p^65p)$  type EUV transitions in  $\text{Sn}^{13+}$ . Subsequently, we apply the method to obtain unique information on the atomic structure of the excited

\*versolato@arcnl.nl

Published by the American Physical Society under the terms of the [Creative Commons Attribution 4.0 International license](https://creativecommons.org/licenses/by/4.0/). Further distribution of this work must maintain attribution to the author(s) and the published article's title, journal citation, and DOI.

configurations  $4p^54d$  in  $\text{Sn}^{14+}$  and  $4p^44d$  in  $\text{Sn}^{15+}$ . Line identifications in  $\text{Sn}^{15+}$  are enabled using the semiempirical Cowan code [30], which allows for adjusting scaling factors applied to radial integrals in order to fit observed spectra using initial preliminary assignments. Identifications of lines in both  $\text{Sn}^{14+}$  and  $\text{Sn}^{15+}$  are further strengthened by line intensity calculations using the collisional-radiative modeling capabilities of the Flexible Atomic Code (FAC) [31]. We compare our obtained level energies with calculations performed with the Fock-Space Coupled-Cluster (FSCC) approach for  $\text{Sn}^{14+}$  [16] and General-purpose Relativistic Atomic Structure Package (GRASP) calculations for  $\text{Sn}^{15+}$  [32]. In this work, we also provide state-of-the-art calculations of  $\text{Sn}^{15+}$  using the configuration-interaction many-body perturbation code AMBiT [33]. Its performance is gauged against published calculations as well as experimental observations.

## II. EXPERIMENT

We performed spectroscopic measurements in the EUV region on tin ions over the range of charge states  $\text{Sn}^{9+}$ – $\text{Sn}^{20+}$  at the FLASH-EBIT facility [34] at the Max Planck Institute for Nuclear Physics in Heidelberg, Germany. FLASH-EBIT employs a pair of superconducting Helmholtz coils to generate a 6-T magnetic field in order to guide and compress the electron beam, with a density of approximately  $10^{11}e^- \text{cm}^{-3}$  (see below), down to a diameter of about  $50 \mu\text{m}$ . A molecular beam of tetra-*i*-propyltin ( $\text{C}_{12}\text{H}_{18}\text{Sn}$ ) was injected into the trap through a two-stage differential pumping system. The tetra-*i*-propyltin molecules are dissociated while crossing the electron beam. The electron beam rapidly ionizes and traps the Sn ions, while the lighter elements leave the trap. By adjusting the acceleration voltage, the electron-beam energy can be set to achieve preferential production of a specific charge state. Subsequently, the electron beam collisionally populates excited states from which the emission is collected.

Extreme-ultraviolet radiation emitted by the highly charged ions in the trap is diffracted by a 1200-lines/mm flat-field, grazing-incidence grating [35] and recorded on a Peltier-cooled charge-coupled device (CCD) sensor. The wavelength range covered by the spectrometer encompasses the 13.5-nm region most relevant to nanolithographic applications. A wavelength range from 12.6–20.8 nm is captured in the observation of light diffraction in first order of the grating, with lines having a full width at half maximum (FWHM) of about 0.03 nm. To achieve the best possible resolution, the camera position was alternatively set such that the 12–17 nm spectral range can be observed in second order where typically a FWHM resolution of about 0.02 nm was achieved. The spectra are corrected for small optical aberrations and background signal before projection onto the dispersive axis of the full CCD image. Corrections for camera sensitivity and grating efficiency are subsequently applied. Wavelength calibration of the spectrometer is performed by injecting oxygen into the trap and observing a set of known  $\text{O}^{2+}$ – $\text{O}^{4+}$  lines [36]. The calibration uncertainty of 0.003 nm (one standard deviation of the residuals) is the dominant contributor to the overall uncertainty budget for determining line centers. Calibration runs were performed on several days during the experimental campaign to combat any potential

significant drift. Line positions found in the first- and second-order-diffraction measurements (see below), performed on different days and under different EBIT settings, agree well within the uncertainty estimates.

Two measurement series are performed, utilizing either the first- or second-order diffraction of the grating. Fluorescence emission from  $\text{Sn}^{12+}$ – $\text{Sn}^{20+}$  is observed by increasing the electron-beam energy in 5-eV steps from 320 to 695 eV while keeping the electron-beam current constant at 20 mA. The light captured on the CCD is integrated for 480 s per electron-beam energy step. In the second-order measurement series, EUV emission from tin ions in charge states 9+ up to 18+ is observed by increasing the energy of the electron beam in 10-eV steps from 210 to 560 eV. The electron-beam current in the second-order measurement series was kept steady at 10 mA. In each of the 36 steps of the electron-beam energy, an EUV spectrum was accumulated with a camera integration time of 1800 s to ensure a sufficient signal-to-noise ratio. In the following, results from the second-order measurement series are described in detail. First-order measurement results are employed for further line identifications in the wavelength range not captured in second order.

## III. GENERAL FEATURES OF THE EUV EMISSION MAPS

A 2D map (wavelength, electron-beam energy) of EUV light intensities is presented in Fig. 1. An initial-charge-state identification is performed by locating known lines in the 2D map. The very bright emission feature near 13.34 nm is the resonant  $4p^6 \ ^1S_0$ – $4p^54d \ ^1P_1$  transition in  $\text{Sn}^{14+}$  [7,37]. At slightly shorter wavelength, lines from  $\text{Sn}^{13+}$  can be identified [6,7,38]. From Fig. 1, it can be seen that the strong emission manifolds belonging to  $4p^64d^m$ –( $4p^54d^{m+1} + 4p^64d^{m-1}4f$ ) transitions in  $\text{Sn}^{9+}$  ( $m = 5$ ) to  $\text{Sn}^{13+}$  ( $m = 1$ ) shift toward shorter wavelength with increasing charge state. EUV emission from these open  $4d$ -subshell ions have been extensively studied in the literature; see, e.g., Refs. [6–9]. Intriguingly, after emptying the  $4d$  subshell at 14-fold charged tin, the strongest transitions for tin ions in charge state 14+ and higher shift back to longer wavelengths.

The emergence and submergence of spectral features at certain electron-beam energies can be understood from considerations of the ionization potentials of tin ions. This procedure allows for the assessment of ranges of electron-beam energies in which tin ions in a specific charge state are the dominant contributors to the EUV spectra. In each of the charge-state bands, the measured spectrum with the highest fluorescence is chosen as the representative spectrum for that charge state. In Fig. 1, the overlaid line spectra (white solid lines) are the corresponding spectra for  $\text{Sn}^{13+}$ ,  $\text{Sn}^{14+}$ , and  $\text{Sn}^{15+}$ . From the figure it is clear that representative spectra are not free of spectral admixtures from Sn ions in adjacent charge states. Fluorescence curves are a way to assess potential admixtures of different charge states. A fluorescence curve represents the intensity of a specific line as a function of electron-beam energy. We project vertical regions of interest from the data as shown in Fig. 1. Several lines per charge state are identified in order to construct a generic fluorescence curve. We choose in the spectral map lines that are preferably isolated, mostly outside of dense spectral regions,

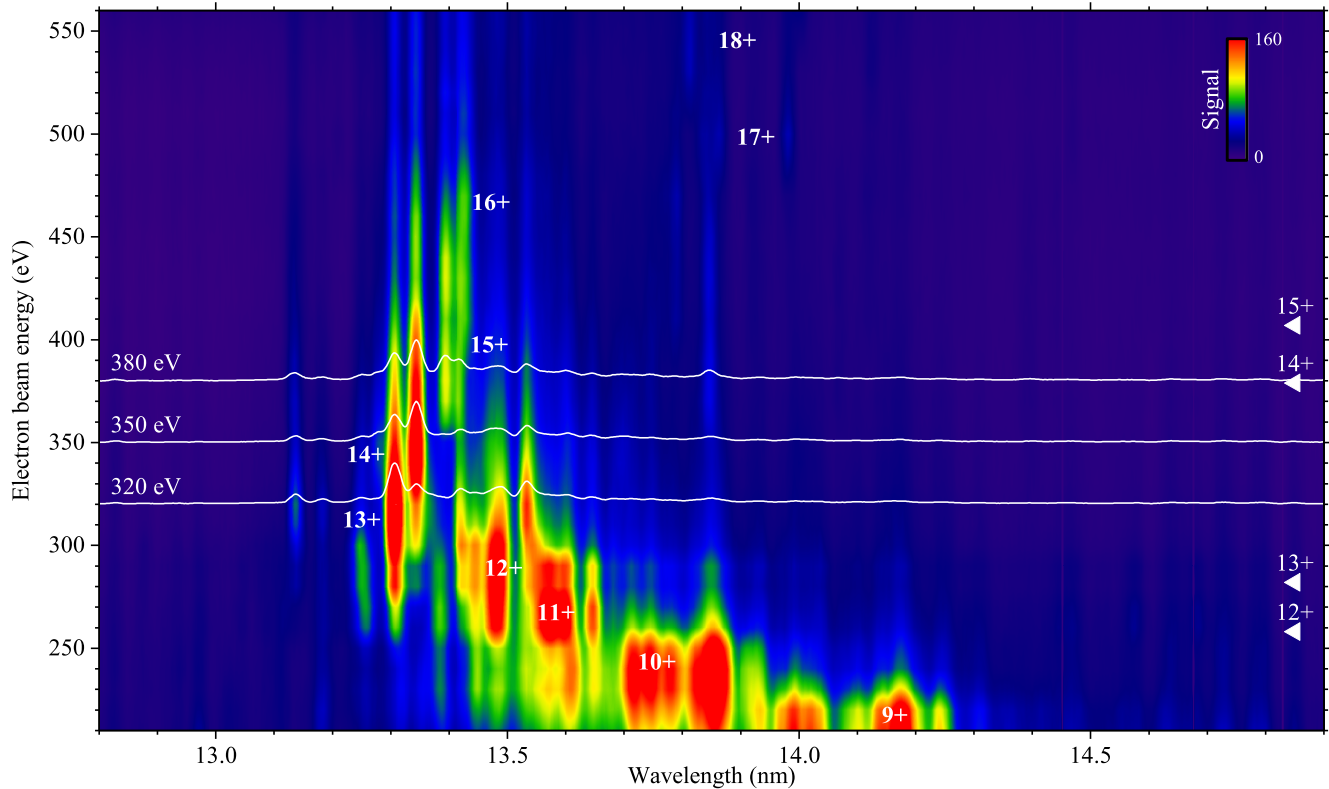


FIG. 1. Spectral intensity map of Sn ions constructed from measurements at the FLASH-EBIT, obtained in second-order diffraction from a 1200-lines/mm grating. The 2D map is produced by interpolating between discrete spectra that are taken at 10 eV electron-beam energy steps. The main features belonging to  $\text{Sn}^{9+}$  to  $\text{Sn}^{18+}$  ions are labeled. The overlaid spectra (white solid lines) at 320, 350, and 380 eV show representative EUV spectra of  $\text{Sn}^{13+}$ ,  $\text{Sn}^{14+}$ , and  $\text{Sn}^{15+}$  ions, respectively, at the peak of their fluorescence curves. The white triangles denote the location of the ionization potential belonging to  $\text{Sn}^{q+}$ .

and compare them critically. It is found that commonly the observed energy dependencies of the line strengths are very similar for all lines associated with a particular charge state. Lines with expected blends of other charge states, showing miscellaneous energy-dependent behavior, were excluded or corrected for contributions from line blending. Individual fluorescence curves are normalized and subsequently averaged such that a generic fluorescence curve per charge is obtained. The normalized fluorescence curves of  $\text{Sn}^{9+}$  to  $\text{Sn}^{18+}$  ions are shown in Fig. 2. In general, the fluorescence from a certain ionic state  $q$  increases rapidly once the electron-beam energy exceeds the ionization potential of the previous charge state  $q - 1$ . Once the ionization potential of the charge state  $q$  is reached, the fluorescent curve belonging to  $q$  is observed to decline. The electron beam produces a strong space charge region in the trap, lowering the actual electron-beam energy in the interaction region in the center of the trap by a current-dependent value [16,39]. This effect however is partially compensated by the trapped positive ions. The net result is typically a lowering of the electron-beam energy by a few eV per mA current [16,39]. Space charge effects have a negligible influence on the onset of the fluorescence curves (cf. Fig. 2). The fluorescence curve of  $\text{Sn}^{15+}$  is different from the other charge states as it shows two peaks instead of one. This can be explained by early production of  $\text{Sn}^{15+}$  out of metastable  $\text{Sn}^{14+}$  levels, similar to the case presented in Ref. [16]. Although weaker, a similarly early onset is also visible for

$\text{Sn}^{16+}$ . The relevance of early ionization via metastable levels as intermediate steps depends on a delicate balance between the lifetimes of said metastable levels and the electron-beam

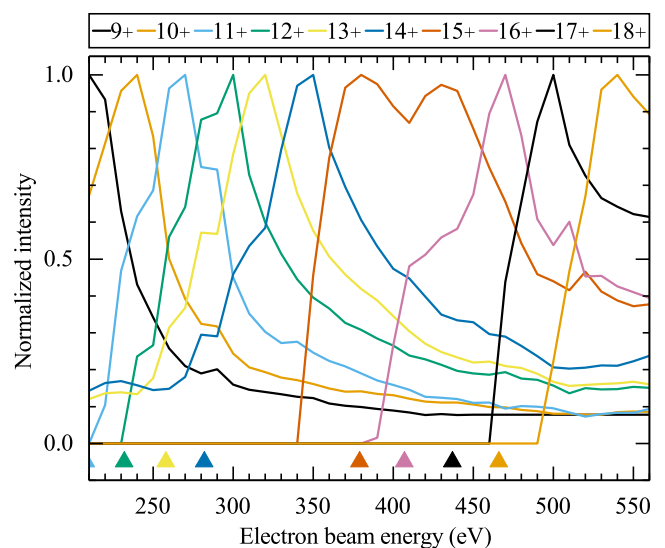


FIG. 2. Normalized intensity of spectral lines belonging to  $\text{Sn}^{q+}$  ( $q = 9-18$ ) along the variation of the set electron-beam energy. The triangles mark the threshold for producing the  $\text{Sn}^{q+}$  ion at the ionization potential of charge state  $q - 1$  [41].

density [40]. These features are well captured by our method below and therefore do not negatively impact it.

The fluorescence curves indicate that a tin spectrum, taken at any single electron-beam energy, contains emission features from a mixture of tin charge states. In the following, we will employ a method to retrieve charge-state-resolved spectra.

#### IV. MATRIX INVERSION

For unraveling blended spectra, such as the ones of  $\text{Sn}^{q+}$  ions, we employ a matrix inversion method for charge-state-resolved EBIT spectral reconstruction. The principle of the method is analogous to that of the subtraction scheme introduced by Lepson *et al.* [27]. In the matrix inversion method it is hypothesized that each row in the 2D map (wavelength, electron-beam energy) of light intensities shown in Fig. 1 in fact represents a linear combination of unique spectra per charge state weighted by their respective fluorescence curve. These spectral maps can thus be represented by a matrix  $\mathbf{E}$  of dimension  $m \times w$ , where  $m$  is the number of spectral scans (electron-beam energy steps) and  $w$  is the number of wavelength bins. The matrix elements contain spectral intensities directly obtained from measurements. Fluorescence curves, such as the ones shown in Fig. 2, span a fluorescence matrix  $\mathbf{F}$  of dimension  $m \times c$ , where  $c$  is the number of distinct charge states in the EBIT spectrum. This overdetermined linear system can be described as

$$\mathbf{F}\mathbf{S} = \mathbf{E}, \quad (1)$$

with  $\mathbf{S}$  containing the charge-state-resolved spectra to be determined. The least-squares solution for this problem is found by utilizing the generalized inverse method [42]. The solution yields the minimum norm of the system and is found by first multiplying Eq. (1) with the transpose of the fluorescence matrix  $\mathbf{F}$ :

$$\mathbf{F}^T \mathbf{F} \mathbf{S} = \mathbf{F}^T \mathbf{E}. \quad (2)$$

The matrix product  $\mathbf{F}^T \mathbf{F}$  is a square matrix and allows for the determination of an inverse, in the case of full column rank of  $\mathbf{F}$  (i.e., when each column is linearly independent). The present experimental data fulfill this requirement. Subsequently, when Eq. (2) is multiplied by this inverse, the solution of matrix  $\mathbf{S}$  is given by

$$\mathbf{S} = (\mathbf{F}^T \mathbf{F})^{-1} \mathbf{F}^T \mathbf{E}. \quad (3)$$

This solution is also referred to as the *left inverse* of this linear system. The resulting matrix  $\mathbf{S}$  has dimensions  $c \times w$ .

The non-negative matrix factorization (NNMF) method [43] provides an alternative route for obtaining matrices  $\mathbf{F}$  and  $\mathbf{S}$ . NNMF enables obtaining the (positive-definite) matrices without any prior knowledge of the system, such as the fluorescence curves. Test fits to our EBIT spectra with the NNMF method were made for comparison with the spectra obtained from matrix inversion. For  $\text{Sn}^{13+}$ , the NNMF spectrum looked very similar; however, a few spurious spectral features emerged when retrieving  $\text{Sn}^{14+}$  and  $\text{Sn}^{15+}$  spectra. Therefore, we do not consider NNMF in the following and accept a few small spurious features in the spectra reconstructed through matrix inversion, cf. Fig. 3, stemming from imperfections in

the fluorescence curves. However, such artifacts can easily be identified and excluded.

#### V. RESULTS AND LINE IDENTIFICATIONS

Charge-state-resolved spectra reconstructed by means of the matrix inversion method are presented in Fig. 3. The direct EBIT spectra at electron-beam energies at which Sn charge states  $\text{Sn}^{13+}$ ,  $\text{Sn}^{14+}$ , and  $\text{Sn}^{15+}$  show maximum fluorescence are included in Fig. 3. From comparison of the results of the matrix inversion with the untreated direct data, it is evident that there exist large admixtures of charge states in the untreated spectra. A detailed analysis of the line identifications of  $\text{Sn}^{13+}$  to  $\text{Sn}^{15+}$  ions is presented, using the case of  $\text{Sn}^{13+}$  ions as a reference as its atomic structure is well known [6,7,38]. An analysis per charge state is laid out after a short introduction to the various atomic structure codes used to perform the line identifications.

The Hartree-Fock method with relativistic corrections incorporated in the RCN-RCN2-RCG chain of the Cowan code [30,44] is used for the calculation of wavelengths of  $4p^6-4p^54d$  and  $4p^5-4p^44d$  transitions in  $\text{Sn}^{14+}$  and  $\text{Sn}^{15+}$  ions, respectively. In addition to the wavelength of a transition, the line intensity is also an important identification tool. For experiments on EBITs, the electron beam may strongly affect specific line intensities, making them deviate strongly from calculated  $gA$  values (multiplicity times the Einstein coefficient); see, e.g., Ref. [39]. Inclusion of such effects requires collisional-radiative modeling (CRm). We used the CRm capabilities available in FAC [31]. CRm calculates the relative population of levels within the atomic structure. The ‘‘line emissivity,’’ presented as luminosity in photons/s, is obtained from the multiplication of the relative population times the Einstein  $A$  coefficient as calculated by FAC [31].

FAC calculations here tend to overestimate level energies in comparison with experiment. Therefore, we have shifted level energies calculated by FAC to match the level energies obtained from the Cowan code. Following the conclusions in Ref. [39], in which electron-beam densities in FLASH-EBIT were investigated under similar conditions, we used a  $10^{11} \text{e}^- \text{cm}^{-3}$  electron-beam density in our CRm calculations. This density is shown to accurately predict the relative intensities of magnetic-dipole to electric-dipole transitions in  $\text{Sn}^{14+}$ . Slight differences in the choice of density and possible polarization-induced emission anisotropies (such as observed, e.g., in recombination measurements in Refs. [45,46]) were investigated and are not expected to affect the final identifications. Cowan and FAC-CRm details specific to  $\text{Sn}^{14+}$  and  $\text{Sn}^{15+}$  ions are discussed in the following subsections. The resulting spectra are individually normalized per charge state. Area-under-the-curve line intensities are normalized to the strongest line for each charge state in order to allow for a straightforward comparison with the normalized line spectra.

##### A. Spectrum of $\text{Sn}^{13+}$

The EUV spectrum of  $\text{Sn}^{13+}$  has been studied previously in plasma discharge sources [6,7,38]. Strong lines between 13.1 and 13.6 nm have been identified as belonging to resonant transitions between levels of the first excited configuration

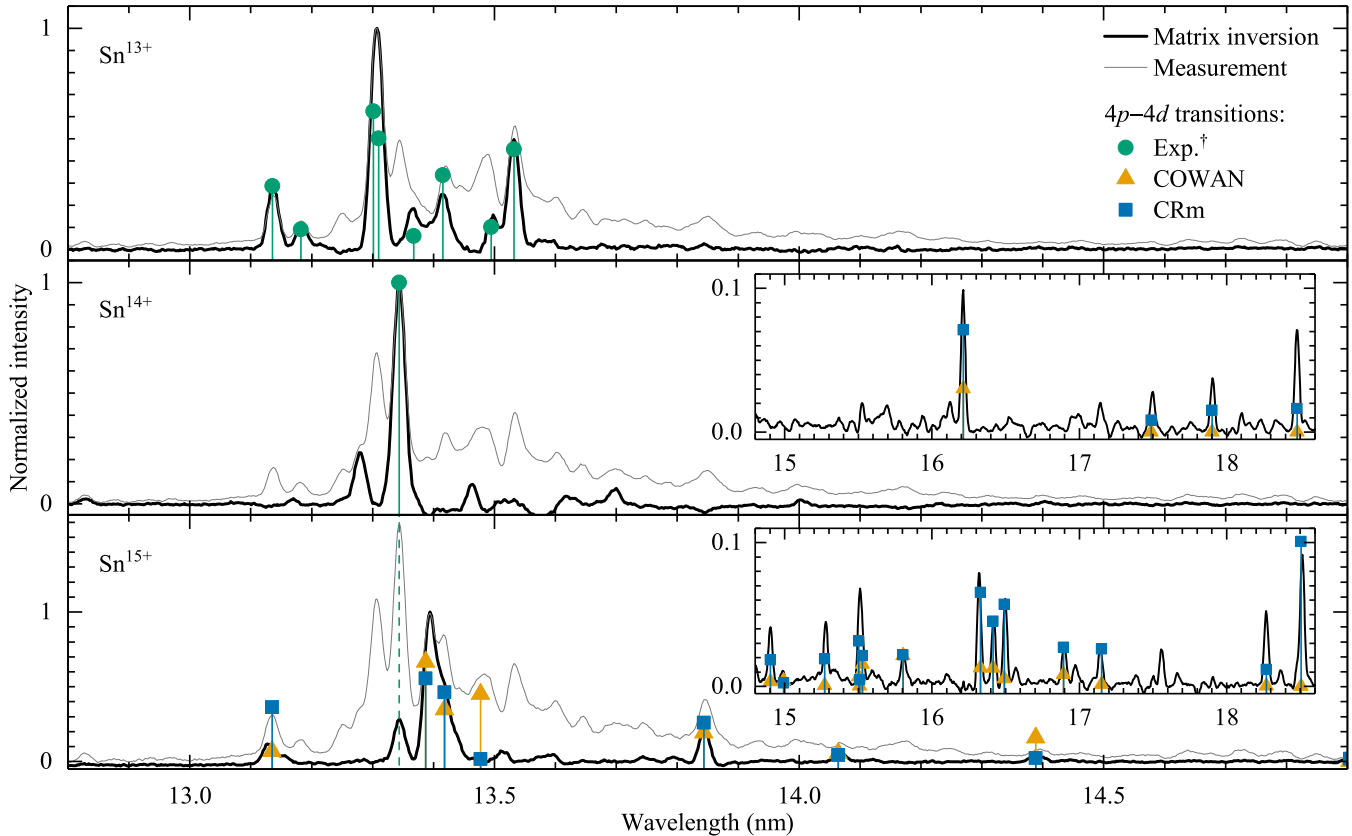


FIG. 3. Charge-state-resolved spectra for Sn charge states  $\text{Sn}^{13+}$ – $\text{Sn}^{15+}$ . Spectra determined with the matrix inversion method (described in Sec. IV) are shown in black. The untreated EBIT spectra are represented by thin gray lines and are identical to the line-out projections in Fig. 1, here normalized to the strongest line feature associated with the respective charge state. <sup>†</sup>The green circular data points represent normalized  $gA$  factors for transitions previously identified in the literature [6,7],  $4p^64d-4p^54d^2$  transitions in  $\text{Sn}^{13+}$  and  $4p^6-4p^54d$  transitions in  $\text{Sn}^{14+}$ . A vertical dashed line at 13.34 nm indicates an artifact; see Sec. V C. The insets in the center and bottom panels show part of the  $\text{Sn}^{14+}$  and  $\text{Sn}^{15+}$  spectra measured in the first-order measurement series. Yellow triangles indicate normalized  $gA$  factors resulting from Cowan code calculations. Normalized emissivity values, calculated by FAC’s CRm module, are shown as blue squares.

$4p^54d^2$  and the  $4p^64d$  ground configuration. The top panel of Fig. 3 shows our untreated (gray line) and matrix-inverted (black) EUV spectrum of  $\text{Sn}^{13+}$ . The matrix-inverted result is in excellent agreement with previous identifications, as shown in Fig. 3 and in Table I. Comparing the matrix-inverted and untreated spectra of  $\text{Sn}^{13+}$  makes clear that spectral analysis solely based on a measurement taken at peak fluorescence for this ion would not provide sufficient detail. This demonstrates and validates the applicability of the method to the measured EBIT spectra. One of the four possible transitions within the  $^2D-4d^2$  ( $^3F$ ) $^2D$  multiplet is not observed (cf. Table I). The transition  $^2D_{3/2}-(^3F)^2D_{5/2}$  may be expected at a wavelength of 13.08 nm. However, according to the Cowan code calculations, it has a too low  $gA$  value to be detected. Also, the  $^2D_{5/2}-4d^2$  ( $^1G$ ) $^2F_{5/2}$  transition predicted at 13.78 nm is not detected as may be expected because this  $\Delta J = 0$  transition is further suppressed by configuration interaction.

### B. Spectrum of $\text{Sn}^{14+}$

The EUV spectrum of  $\text{Sn}^{14+}$  consists of a few resonance lines. Two lines at approximately 13.34 and 16.21 nm have been observed previously [6,7,37], and are observed in our spectra as well. Additionally, three new lines in the

17–19 nm range are identified. Line positions and assignments of these five  $\text{Sn}^{14+}$  transitions are presented in Table II. The assigned transitions stem from levels 2, 3, and 6 (see Table III), which are mainly of character  $^3P_1$ ,  $^3P_2$ , and  $^1D_2$ , respectively. Excellent agreement is obtained with the fine structure determined in Ref. [16], where the fine structure of the  $4p^54d$  configuration was studied by the observation of magnetic dipole transitions in the optical regime. The level energy differences between levels 2–3 and 2–6 have been measured directly. They form Ritz combinations with transitions found in the EUV. Two of the newly assigned EUV lines in the 17–19 nm range (originating from upper levels 3 and 6) have very small  $gA$  values (on the order of  $1000 \text{ s}^{-1}$ ) as is to be expected for  $\Delta J = 2$  transitions. Notwithstanding that, these lines are observed in the EBIT spectrum because of the strongly enhanced population of their upper levels as indicated by our CRm calculations.

Fock-Space Coupled-Cluster (FSCC) predictions for the structure of  $\text{Sn}^{14+}$  [16], shown in Table III, are in excellent agreement with our identifications with a root-mean-square difference with experiment below 0.1%.

Through a semiempirical adjusting of scaling factors, the Cowan code enables evaluating level energies of  $\text{Sn}^{14+}$  to a high accuracy. The level energies of the  $4s^24p^54d$

TABLE I. Comparison of observed wavelengths of EUV lines in  $\text{Sn}^{13+}$  with literature values. Transitions stem from strongly mixed upper levels associated with the  $4p^5 4d^2$  configuration (denoted by  $4d^2$ ),  $4p^6 4f$ , and  $4p^6 5p$  decaying to the ground configuration  $4p^6 4d$   $^2D_3$ . Wave-function compositions of these mixed levels can be found in Ref. [7]; only the leading term is shown. Wavelength and normalized intensities (Int.) obtained in this work originate from fits to the spectrum. Superscripts on wavelengths indicate blended (bl) lines.

Transition	Wavelength (nm)		Int.
	Literature	Experiment	
$^2D_{3/2}-5p\ ^2P_{3/2}$	12.1339 [6]		
$^2D_{5/2}-5p\ ^2P_{3/2}$	12.3316 [6]	12.334	41
$^2D_{3/2}-5p\ ^2P_{1/2}$	12.5065 [6]	12.519	51
$^2D_{3/2}-4d^2\ (^3F)^2D_{3/2}$	13.1358 [6]	13.137	389
	13.1361 [38]		
$^2D_{3/2}-4d^2\ (^3P)^2P_{3/2}$	13.1821 [7]	13.184	116
$^2D_{5/2}-4d^2\ (^1G)^2F_{7/2}$	13.3014 [6]	13.301 <sup>bl</sup>	586
	13.3020 [38]		
$^2D_{5/2}-4d^2\ (^3F)^2D_{5/2}$	13.3102 [6]	13.304 <sup>bl</sup>	1 000
	13.3105 [38]		
$^2D_{5/2}-4d^2\ (^3F)^2D_{3/2}$	13.3675 [6]	13.367	275
$^2D_{5/2}-4d^2\ (^3P)^2P_{3/2}$	13.4154 [7]	13.415	441
$^2D_{3/2}-4d^2\ (^3P)^2P_{1/2}$	13.4943 [7] <sup>a</sup>	13.498	170
$^2D_{3/2}-4d^2\ (^1G)^2F_{5/2}$ <sup>b</sup>	13.5318 [6]	13.532	711
	13.5315 [38]		

<sup>a</sup>Tentative assignments from Ref. [7].

<sup>b</sup>The dominant term is indicated to be  $4f\ ^2F_{5/2}$  [7].

configuration of  $\text{Sn}^{14+}$  are optimized using configuration interaction between the following configurations:  $4s^2 4p^5 5d$ ,  $4s^2 4p^5 5s$ ,  $4s 4p^5 4d^2$ ,  $4s 4p^6 4f$ ,  $4s^2 4p^3 4d^3$ ,  $4s^2 4p^4 4d 4f$ ,  $4s^2 4p^5 5g$ ,  $4p^5 4d^3$ ,  $4p^6 4d 4f$ , and  $4s 4p^5 4f^2$ . The final Cowan scaling factors are presented in Table IV, with level energies provided in Table III.

There are several other lines observed in the vicinity of the main peak at 13.34 nm in the  $\text{Sn}^{14+}$  spectrum. These transitions do not belong to the  $4p-4d$  transition array. In particular, the line at 13.28 nm stands out. These additional lines may originate from transitions into the excited  $4p^5 4d$  configuration out of the strongly mixing  $4p^5 4f$  and  $4p^4 4d^2$  configurations. There exist many transitions connecting these excited configurations, which prohibits a unique assignment since both expected position and line strength are strongly affected by the effects of configuration interaction. A qualitative study of the emission intensities stemming from FAC-CRM calculations tentatively suggests that the two stronger lines observed at 13.28 and 13.46 nm may be due to, respectively,  $J = 4-5$  and  $J = 3-4$  transitions in the  $4p^5 4d-4p^4 4d^2$  manifold. Similar transitions in the same wavelength range have been observed in charge exchange spectroscopy studies of  $\text{Sn}^{15+}$  ions colliding with He [47].

The influence of the redistribution of level populations by the EBIT beam on the observed line intensity has also been observed in transitions between fine-structure levels of the  $4p^5 4d$  configuration [16]. In Ref. [16], the strongest line at 297.7 nm ( $^3P_2-^3D_3$ , intensity of 211) has a  $gA$  factor of 981, while a neighboring line at 302.9 nm ( $^3D_1-^3D_2$ ) with a three times higher  $gA$  factor of 2597 is detected with a more than

tenfold lower intensity of 15. CRM calculations show that population of the  $^3D_3$  level is strongly preferred. This leads to an inverted emissivity ratio of almost 10 to 1 instead of 1 to 10 for these transitions, in agreement with the measurements.

### C. Spectrum of $\text{Sn}^{15+}$

$\text{Sn}^{15+}$ , with a bromine-like ground-state configuration ( $[\text{Ar}]3d^{10}4s^2 4p^5$ ), has received little attention thus far. Its EUV spectrum in the wavelength range near 13.5 nm consists of one strong emission feature along with several weaker lines; cf. Fig. 3. These features are expected to stem from  $4p^5-4p^4 4d$  transitions. The peak at 13.344 nm belongs to  $\text{Sn}^{14+}$  and is the strongest line in the EBIT measurements. Its contribution is seen to be incompletely removed by the method. It is the only such artifact apparent in the current spectra. The untreated spectra taken at peak fluorescence for  $\text{Sn}^{14+}-\text{Sn}^{16+}$  are shown in the inset in the bottom panel of Fig. 3. This inset highlights the difficulty of identifying the (unresolved) lines belonging to  $\text{Sn}^{15+}$  from observing line intensity changes in the untreated spectra alone. The matrix inversion method is shown to resolve the line features of the  $\text{Sn}^{15+}$  ion.

To enable the identification of  $\text{Sn}^{15+}$  lines (see Table II), the Hartree-Fock method with relativistic corrections (HFR) incorporated in the RCN-RCN2-RCG chain of the Cowan code was used for *ab initio* calculations of wavelengths arising from  $4s^2 4p^5-4s^2 4p^4 4d$  transitions. The following set of odd-symmetry configurations is considered:  $4s 4p^5 4d$ ,  $4s 4p^4 4d 4f$ ,  $4s^2 4p^4 4f$ ,  $4s^2 4p^3 4d^2$ ,  $4s^2 4p^3 4f^2$ ,  $4p^5 4d^2$ ,  $4p^5 4f^2$ , and  $4p^6 4f$ . For the even symmetry, the excited  $4s^2 4p^4 4d$ ,  $4s^2 4p^3 4d 4f$ ,  $4s^2 4p^2 4d^3$ ,  $4s^2 4p^2 4d 4f^2$ ,  $4s 4p^6$ ,  $4s 4p^5 4f$ ,  $4s 4p^3 4d^2 4f$ ,  $4s 4p^4 4d^2$ ,  $4s 4p^4 4f^2$ ,  $4p^6 4d$ ,  $4p^4 4d^3$ , and  $4p^5 4d 4f$  configurations are included. The HFR values are improved on the basis of known data for Br-like  $\text{Mo}^{7+}$  [48]. This is the heaviest system in the Br-like isoelectronic sequence for which the  $4s^2 4p^4 4d$  level energies were found from an analysis of  $4s^2 4p^5-4s^2 4p^4 4d$  transitions [48].

The  $^2P$  term splitting of the ground-state configuration  $4s^2 4p^5$  of  $\text{Sn}^{15+}$  was predicted to be 78 358  $\text{cm}^{-1}$  [49,50] on the basis of a larger set of isoelectronic data including  $\text{Pd}^{11+}$  [51],  $\text{Ag}^{12+}$  [52], and  $\text{Cd}^{13+}$  [53].

Starting out from this initial set of parameters, iterative refinement of the parameters allows for identification of 20 lines belonging to  $\text{Sn}^{15+}$  as  $4s^2 4p^5-4s^2 4p^4 4d$  transitions and 17 level energies of the  $4s^2 4p^4 4d$  configuration along with the  $4s^2 4p^5\ ^2P$  ground term splitting. Our value of 78 300(60)  $\text{cm}^{-1}$  for the  $^2P$  term splitting is in excellent agreement with predictions.

A Cowan code fit to the available level energies to obtain optimal energy parameters leads to a root-mean-square deviation from experimental level energies of 302  $\text{cm}^{-1}$ . The wavelength calibration uncertainty is approximately 150  $\text{cm}^{-1}$ . The final results of the optimization procedure are listed in Table III. The electrostatic energy parameters for the excited configurations were scaled by a factor 0.85 relative to their *ab initio* values while the spin-orbit parameters were not scaled. All configuration-interaction parameters in both parity systems were scaled by 0.85 except for the interaction

TABLE II. Line transitions in  $\text{Sn}^{14+}$  and  $\text{Sn}^{15+}$  determined from fits to the spectra. Superscripts on line wavelengths indicate blended (bl), broad (br), or weak (w) lines. Starred (\*) lines feature in the construction of the fluorescence curves. Line positions beyond 17 nm stem from measurements in first-order diffraction. Below 17 nm, line positions are established from second-order diffraction. Normalized intensities stem from the area-under-the-curve of fits to lines observed in the first-order diffraction. Normalized emissivities from FAC's CRm module are also presented. Transitions are of type  $4p^m-4p^{m-1}4d$  ( $m = 6, 5$  for respectively  $\text{Sn}^{14+}$  and  $\text{Sn}^{15+}$ ); listed numbers refer to levels described in Table III.  $gA$  factors stem from Cowan code calculations, except for transitions 0–3 and 0–6 in  $\text{Sn}^{14+}$ , which are calculated by FAC.

Ion	Wavelength (nm)		Intensity	$gA$ (1/s)	Emissivity	Transition	Terms
	Experiment	Cowan					
14+	13.344*	13.343	1 000	$1.8 \times 10^{12}$	1 000	0–12	$^1S_0-^1P_1$
	13.3431 [7]						
	13.3435 [37]						
	16.212	16.214	137	$5.5 \times 10^{10}$	71	0–8	$^1S_0-^3D_1$
	16.2103 [37]						
	17.497		54	$1.2 \times 10^3$	8	0–6	$^1S_0-^1D_2$
	17.905		63	$1.6 \times 10^3$	15	0–3	$^1S_0-^3P_2$
	18.478	18.480	130	$1.3 \times 10^8$	16	0–2	$^1S_0-^3P_1$
15+	13.129	13.135	159	$3.0 \times 10^{11}$	654 <sup>a</sup>	0–20	$^2P_{3/2}-^2D_{5/2}$
	13.393	13.387	1 000	$2.9 \times 10^{12}$	1 000	0–19	$^2P_{3/2}-^2D_{5/2}$
	13.416	13.418	502	$1.5 \times 10^{12}$	834	0–18	$^2P_{3/2}-^2P_{3/2}$
		13.477			$2.0 \times 10^{12}$	31	1–22
	13.844*	13.844	334	$8.4 \times 10^{11}$	469	0–17	$^2P_{3/2}-^2S_{1/2}$
	14.068	14.064	89	$2.4 \times 10^{11}$	77	0–16	$^2P_{3/2}-^2D_{3/2}$
	14.384 <sup>br</sup>	14.388	13	$7.0 \times 10^{11}$	42	1–21	$^2P_{1/2}-^2P_{1/2}$
	14.903	14.904	59	$1.5 \times 10^{10}$	33	0–15	$^2P_{3/2}-^2D_{5/2}$
	14.989 <sup>w</sup>	14.993	16	$1.7 \times 10^{10}$	4	1–18	$^2P_{1/2}-^2P_{3/2}$
	15.278	15.272	53	$3.6 \times 10^9$	34	0–14	$^2P_{3/2}-^2F_{5/2}$
	15.510 <sup>bl</sup>	15.503	119	$2.9 \times 10^{10}$	57	0–13	$^2P_{3/2}-^2D_{5/2}$
	15.510 <sup>bl</sup>	15.510	119	$1.1 \times 10^9$	9	0–12	$^2P_{3/2}-^4P_{3/2}$
	15.528 <sup>bl</sup>	15.527	120	$6.7 \times 10^{10}$	39	1–17	$^2P_{1/2}-^2S_{1/2}$
	15.811	15.805	42	$9.3 \times 10^{10}$	40	1–16	$^2P_{1/2}-^2D_{3/2}$
	16.320	16.330	140	$5.6 \times 10^{10}$	118	0–10	$^2P_{3/2}-^4P_{5/2}$
	16.421	16.414	81	$5.5 \times 10^{10}$	82	0–9	$^2P_{3/2}-^4F_{3/2}$
	16.498	16.492	103	$2.4 \times 10^{10}$	103	0–8	$^2P_{3/2}-^4F_{5/2}$
	16.897	16.894	56	$3.6 \times 10^{10}$	49	0–6	$^2P_{3/2}-^4P_{1/2}$
	17.143	17.152	61	$5.9 \times 10^9$	47	0–5	$^2P_{3/2}-^2D_{3/2}$
	18.269	18.271	121	$1.5 \times 10^9$	21	0–4	$^2P_{3/2}-^4D_{1/2}$
	18.513*	18.507	225	$4.3 \times 10^8$	182	0–3	$^2P_{3/2}-^4D_{5/2}$

<sup>a</sup>High emissivity resulting from a larger  $gA$  factor calculated by FAC relative to that calculated with the Cowan code; see Sec. V C.

between  $4s^24p^44d$  and  $4s4p^6$  configurations which was varied as shown in Table IV. The scaling factors for the  $4s^24p^44d$  configuration are in agreement with the isoelectronic trends for the sequence  $\text{Y}^{4+}$  [54],  $\text{Zr}^{5+}$  [55],  $\text{Nb}^{6+}$  [56], and  $\text{Mo}^{7+}$  [48], once these previous spectra are fitted with the same set of interacting configurations as used for  $\text{Sn}^{15+}$ . Several key Cowan scaling factors are presented along the Br-like isoelectronic sequence in Fig. 4. Only levels with  $J \leq 5/2$  are included because of the unavailability of level energies for levels with  $J > 5/2$  in  $\text{Nb}^{6+}$ ,  $\text{Mo}^{7+}$ , and  $\text{Sn}^{15+}$ .

The Cowan fit to the experimental data yields  $gA$  factors that can be compared to experimental line intensities. Four transitions with high  $gA$  factors are expected around 13.4 nm. This quartet includes three lines to the ground state from upper levels 18, 19, and 20; cf. Table III. The fourth transition originates from level 22, the highest excited level of the  $4p^54d$  configuration, which decays to the  $^2P_{1/2}$  ground level. Despite its large  $gA$  factor, this transition is not observed in the EBIT spectrum. CRm calculations show that the population of this

upper level 22 is significantly smaller than that of neighboring levels, resulting in a low emissivity for this transition which is in line with our observations.

Typically, we find  $gA$  values obtained from Cowan and FAC to be consistent within a factor of two. One exception is the  $gA$  factor for the transition from level 20 ( $^2D_{5/2}$ ) to the ground state. To understand this further, the transition is compared to the transition to the ground state from  $^2D_{5/2}$  level 19 which is rather similar in wave-function composition and shows no large differences in  $gA$  value between the two codes. The corresponding lines have a measured intensity ratio of 0.16 (transition 20–0/19–0), which is well explained by a  $gA$  factor ratio of 0.10 ( $3.0 \times 10^{11} \text{ s}^{-1}/2.9 \times 10^{12} \text{ s}^{-1}$ ) obtained from Cowan's code after a semiempirical fitting of the experimental line positions. The  $gA$  ratio using HFR standard scaling, before any fitting, is however 1.8 ( $2.2 \times 10^{12}/1.2 \times 10^{12}$ ), not too distinct from a value of 0.7 obtained from FAC calculations. It is also similar to a GRASP calculation indicating a ratio of 1.2 [32,57].

TABLE III. Energy levels of  $\text{Sn}^{14+}$  and  $\text{Sn}^{15+}$ . Energy levels under Experiment are determined from wavelengths shown in Table II, and in addition the Cowan results from the fit to experimental data are listed. Furthermore, theoretical level energies of  $\text{Sn}^{14+}$  are calculated by FSCC (reproduced from Ref. [16]), and by GRASP in the case of  $\text{Sn}^{15+}$  (reproduced from Ref. [32]) as well as by AMBIT.  $\text{Sn}^{15+}$  levels with  $J > 5/2$  are not listed as transitions from these levels are not observed in our spectra. Up to three components of the eigenvector composition are listed for each configuration.

Ion	Config.	Level	Level energy ( $\text{cm}^{-1}$ )			$J$	Percentage eigenvector composition				
			Experiment	Cowan	FSCC [16]						
14+	$4p^6$	0	0	0	0	0	$^1S$				
		$4p^54d$	1		532 121	531 833	0	98% ( $^2P$ ) $^3P$			
		2	541 212	541 118	540 795	1	89% ( $^2P$ ) $^3P$	9% ( $^2P$ ) $^3D$			
		3	558 523	558 571	558 339	2	63% ( $^2P$ ) $^3P$	30% ( $^2P$ ) $^3D$	5% ( $^2P$ ) $^3F$		
		4	560 487 <sup>a</sup>	560 438	560 042	3	69% ( $^2P$ ) $^3F$	21% ( $^2P$ ) $^1F$	9% ( $^2P$ ) $^3D$		
		5		563 501	561 822	4	98% ( $^2P$ ) $^3F$				
		6	571 490	571 828	571 047	2	44% ( $^2P$ ) $^1D$	33% ( $^2P$ ) $^3F$	11% ( $^2P$ ) $^3P$		
		7	592 103 <sup>a</sup>	591 945	592 565	3	63% ( $^2P$ ) $^3D$	35% ( $^2P$ ) $^1F$			
		8	616 892	616 753	617 525	1	84% ( $^2P$ ) $^3D$	8% ( $^2P$ ) $^3P$	5% ( $^2P$ ) $^1P$		
		9		632 893	632 338	2	58% ( $^2P$ ) $^3F$	32% ( $^2P$ ) $^1D$	7% ( $^2P$ ) $^3D$		
		10		649 941	649 997	2	50% ( $^2P$ ) $^3D$	24% ( $^2P$ ) $^3P$	21% ( $^2P$ ) $^1D$		
		11		658 062	658 463	3	43% ( $^2P$ ) $^1F$	29% ( $^2P$ ) $^3F$	26% ( $^2P$ ) $^3D$		
	12	749 429	749 449	750 368	1	92% ( $^2P$ ) $^1P$	5% ( $^2P$ ) $^3D$	1% ( $^2P$ ) $^3P$			
Ion	Config.	Level	Level energy ( $\text{cm}^{-1}$ )				$J$	Percentage eigenvector composition <sup>b</sup>			
			Experiment	Cowan	GRASP [32]	AMBIT					
15+	$4p^5$	0	0	0	0	0	3/2	$^2P$			
			1	78 300	78 300	77 573	78 391	1/2	98% $^2P$		
		$4p^44d$	2	540 160	539 988	552 900	540 618	3/2	56% ( $^3P$ ) $^4D$	13% ( $^3P$ ) $^4P$	12% ( $^1D$ ) $^2D$
		3		540 344	552 374	540 799	5/2	68% ( $^3P$ ) $^4D$	8% ( $^1D$ ) $^2D$	7% ( $^3P$ ) $^4F$	
		4	547 380	547 330	561 866	547 849	1/2	38% ( $^3P$ ) $^4D$	25% ( $^1D$ ) $^2P$	20% ( $^3P$ ) $^2P$	
		5	583 330	583 015	595 347	585 107	3/2	31% ( $^1S$ ) $^2D$	23% ( $^3P$ ) $^4P$	18% ( $^3P$ ) $^4F$	
		6	591 820	591 934	610 436	593 334	1/2	64% ( $^3P$ ) $^4P$	18% ( $^3P$ ) $^2P$	10% ( $^1D$ ) $^2P$	
		7		604 177	616 910	604 006	1/2	60% ( $^3P$ ) $^4D$	14% ( $^1D$ ) $^2P$	12% ( $^3P$ ) $^4P$	
		8	606 130	606 367	616 888	607 902	5/2	49% ( $^3P$ ) $^4F$	28% ( $^1S$ ) $^2D$	11% ( $^3P$ ) $^4P$	
		9	608 980	609 246	623 121	610 977	3/2	41% ( $^3P$ ) $^4F$	23% ( $^3P$ ) $^4P$	16% ( $^1D$ ) $^2D$	
		10	612 750	612 365	628 411	615 164	5/2	34% ( $^3P$ ) $^4P$	21% ( $^3P$ ) $^2F$	19% ( $^3P$ ) $^4F$	
		11		620 095	634 622	620 638	3/2	31% ( $^3P$ ) $^4D$	16% ( $^1D$ ) $^2D$	15% ( $^1D$ ) $^2P$	
		12	644 750	644 728	660 531	645 662	3/2	29% ( $^3P$ ) $^4P$	24% ( $^1D$ ) $^2P$	22% ( $^3P$ ) $^2P$	
		13	644 750	645 021	661 069	646 848	5/2	29% ( $^1D$ ) $^2D$	28% ( $^1D$ ) $^2F$	15% ( $^3P$ ) $^2D$	
		14	654 540	654 802	670 067	656 739	5/2	50% ( $^3P$ ) $^2F$	22% ( $^3P$ ) $^4P$	17% ( $^1D$ ) $^2F$	
		15	671 010	670 948	690 149	673 929	5/2	36% ( $^1D$ ) $^2D$	34% ( $^1D$ ) $^2F$	11% ( $^3P$ ) $^4P$	
		16	710 810	711 019	723 750	713 461	3/2	34% ( $^1S$ ) $^2D$	22% ( $^1D$ ) $^2P$	20% ( $^3P$ ) $^4F$	
		17	722 330	722 341	760 578	724 932	1/2	67% ( $^1D$ ) $^2S$	15% ( $^2S$ ) $^2S$	7% ( $^1D$ ) $^2P$	
		18	745 420	745 278	765 637	748 655	3/2	39% ( $^3P$ ) $^2P$	21% ( $^1D$ ) $^2P$	21% ( $^1D$ ) $^2D$	
		19	746 660	746 998	763 991	750 125	5/2	50% ( $^3P$ ) $^2D$	25% ( $^1S$ ) $^2D$	13% ( $^1D$ ) $^2D$	
		20	761 670	761 325	780 364	764 672	5/2	36% ( $^1S$ ) $^2D$	17% ( $^3P$ ) $^2D$	16% ( $^3P$ ) $^2F$	
		21	773 520	773 307	793 949	775 883	1/2	45% ( $^3P$ ) $^2P$	42% ( $^1D$ ) $^2P$	8% ( $^1D$ ) $^2S$	
	22		820 293	840 862	823 384	3/2	50% ( $^3P$ ) $^2D$	22% ( $^1S$ ) $^2D$	9% ( $^3P$ ) $^2P$		

<sup>a</sup>Level energies were determined in Ref. [16] relative to level 2 by measuring transitions 3–7, 4–7, and 6–7.

<sup>b</sup>All components belong to the  $4p^44d$  configuration except for level 17, where the second component belongs to  $4s4p^6$ .

TABLE IV. Cowan code Hartree-Fock with relativistic corrections (HFR) and least-squares-fitted (LSF) parameter values of the  $4s^24p^54d$  and  $4s^24p^44d$  configurations respectively in  $\text{Sn}^{14+}$  and  $\text{Sn}^{15+}$ . All parameters are given in units of  $\text{cm}^{-1}$ . One-standard-deviation uncertainties are given in brackets.

Parameter	$\text{Sn}^{14+}$			$\text{Sn}^{15+}$		
	HFR <sup>a</sup>	LSF	LSF/HFR <sup>b</sup>	HFR <sup>a</sup>	LSF	LSF/HFR <sup>b</sup>
$E_{\text{average}}$	632 080	629 400(327)	−2 680	671 287	669 270(98)	−2 017
$F^2(4p, 4p)$				133 798	123 714(1 216)	0.925(9)
$\zeta(4p)$	50 300	51 428(751)	1.022(15)	51 881	53 251(187)	1.026(4)
$\zeta(4d)$	5 348	5 823(228)	1.089(43)	5 602	5 788(150)	1.033(27)
$F^2(4p, 4d)$	125 410	115 494(1 707)	0.921(14)	127 338	117 332(1 054)	0.921(8)
$G^1(4p, 4d)^c$	158 897	142 206(674)	0.895(4)	161 200	144 568(273)	0.897(2)
$G^3(4p, 4d)^c$	100 630	90 060(427)	0.895(4)	102 264	91 712(173)	0.897(2)
${}^1D(4s4d, 4p4p)^d$				167 595	147 825(787)	0.882(5)
$\sigma$		279			302	

<sup>a</sup>Average energies are adjusted so that the energy of the ground level is zero in calculations with 0.85 scaling of all electrostatic parameters.

<sup>b</sup>The value given for  $E_{\text{average}}$  represents the difference between LSF and HFR value.

<sup>c</sup>Parameters are tied at their HFR ratio at the fitting.

<sup>d</sup>Interaction between  $4s^24p^44d$  and  $4s^14p^6$  configurations in  $\text{Sn}^{15+}$ .

The here-established quenching of oscillator strength of the 20–0 transition demonstrates the sensitivity of  $gA$  values to the exact wave-function composition.

The quality of the obtained complete set of Cowan code level energies is further illustrated by the identification of a particularly bright optical line observed in Ref. [16] at EBIT settings compatible with the production of  $\text{Sn}^{15+}$ . This line, predicted and observed at 538 nm, can be straightforwardly assigned to the yrast-type  $({}^3P)4D_{7/2} - ({}^3P)4F_{9/2}$  transition within the  $4p^54d$  configuration.

#### AMBIT

We have calculated the energies of the  $4p-4d$  transitions of  $\text{Sn}^{15+}$  using the particle-hole CI+MBPT (combination of configuration interaction and many-body perturbation theory [58]) method implemented in AMBIT [33]. Detailed expla-

nations of the method, including formulas, can be found in Ref. [59], while the particle-hole formalism is introduced in Ref. [60]. Below, we present specific details of relevance to the current calculation.

We begin by generating the single-electron wave functions  $|i\rangle$  by solving the self-consistent Dirac-Hartree-Fock (DHF) equations

$$\hat{h}_{\text{DHF}}|i\rangle = \varepsilon_i|i\rangle,$$

where  $\hat{h}_{\text{DHF}}$  is the Dirac-Hartree-Fock operator (in atomic units):

$$\hat{h}_{\text{DHF}} = c\boldsymbol{\alpha} \cdot \mathbf{p} + (\beta - 1)c^2 + V_{\text{DHF}}(r),$$

where  $V_{\text{DHF}}(r)$  is the mean potential generated by the electrons included in the Hartree-Fock procedure plus the nuclear potential with finite-size corrections. This calculation is started from the  $V^{N-1}$  approximation, including the partially occupied  $4p^4$  shell by scaling the filled shell. We also include additional terms to account for the Breit interaction and the Lamb shift, including the Uehling potential vacuum energy corrections and electron self-energy corrections [61–63].

Multielectron wave functions are produced by taking Slater determinants of these  $|i\rangle$ . For each electronic configuration, we take all Slater determinants with a given total angular momentum projection  $M$  and diagonalize them over  $\hat{\mathbf{J}}^2$  to form a basis of configuration-state functions (CSFs) with definite total angular momentum  $J$  and projection  $M$  to be used in CI.

We now set the Fermi level above the  $4s$  orbital, so there are effectively five valence electrons in  $\text{Sn}^{15+}$ . The  $4s$  level is considered as a hole state, and we allow hole-particle excitations including this orbital. Note that at CI level this is exactly equivalent to having seven valence electrons (including the  $4s^2$  shell in the valence set), provided that the same configurations are included in the CI. However, from a MBPT perspective it reduces the overall size of subtraction diagrams [60]. The CI space consists of configurations generated by single and double electron excitations up to  $8spdf$  orbitals from the reference configurations  $4p^5$ ,  $4p^44d$ ,  $4p^34d^2$ ,  $4p^24d^3$ ,  $4p^45s$ , and  $4s^{-1}4p^6$ . Additional configurations consisting of

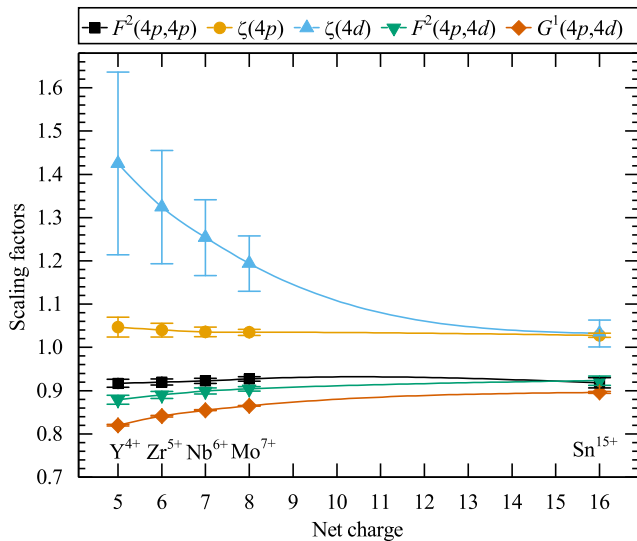


FIG. 4. Empirical adjustments of scaling factors in the Cowan code calculations along the Br-like isoelectronic sequence (for details see text). Spline fits are drawn to guide the eye.

a particle-hole excitation from the reference set along with a valence electron excitation were also included. In order to reduce the size of the CI calculation, without sacrificing accuracy, the “emu CI” technique described in Ref. [64] is used. To summarize, of the  $N$  CSFs in the CI basis, only a much smaller number  $N_s$  of usually lower energy CSFs will dominate the expansion of the states of interest. For those important configurations, all interactions are accounted for. However, interactions between configurations outside of this smaller set are neglected. To achieve this, we place the  $N_s$  important CSFs in the top of the CI matrix and set off-diagonal elements that correspond to interactions between higher energy states to 0. As an example, for the even-parity  $J = 7/2$  configurations we had  $N = 407\,271$  and  $N_s = 40\,704$ , reducing the number of calculated elements of the CI matrix by a factor of five.

Core-valence interactions involving the other core levels (up to  $3spd$ ) are small since the core and valence electrons are well separated in energy. In the CI+MBPT method these are treated perturbatively up to second order by modifying the Slater integrals [58]. In the diagrammatic expansion we included virtual orbitals up to  $30spdfg$  and all orbitals that were frozen at CI level.

The AMBiT calculations are done at a level similar to previous work on  $\text{Sn}^{7+}$  [16]. This case also has five valence electrons; however, we are now interested in high-energy transitions between configurations, rather than levels within a multiplet ( $4d^5$  in the case of  $\text{Sn}^{7+}$ ). The results are shown in Table III. We find a systematic offset in the AMBiT  $4p^44d$  energy levels compared to experiment of  $2100(900)\text{ cm}^{-1}$ , which originates from the relaxation of the  $4p$  orbitals in the different configurations and is not completely accounted for by the CI and MBPT approach. Our overall relative accuracy is  $\sim 0.3\%$ , which compares favorably with the previous theory  $2.6\%$  [32]; cf. Table III. The accuracy of AMBiT very nearly enables the direct identification of the observed lines without the need of semiempirical scaling parameters as in the case of the Cowan code, particularly so when correcting for the observed systematic shifts in level energies.

## VI. CONCLUSION

We study the extreme-ultraviolet spectra near  $13.5\text{ nm}$  wavelength of  $\text{Sn}^{13+}$ – $\text{Sn}^{15+}$  ions as measured in an electron-beam ion trap. A matrix inversion method enables the reevaluation of resonance transitions in  $\text{Sn}^{13+}$  and  $\text{Sn}^{14+}$  ions. In the latter ion, three additional EUV lines confirm its previously established level structure.

For  $\text{Sn}^{15+}$  we present the first line spectrum and use the Cowan code for line identification and assignments. These assignments are furthermore strengthened by the collisional-radiative modeling capabilities of the Flexible Atomic Code, thus including line emissivities in the identification process by modeling the EBIT plasma. Using the 20 lines identified, we establish 17 level energies of the  $4p^44d$  configuration as well as the fine-structure splitting of the  $4p^5$  ground state. We find that strong  $4p$ – $4d$  transitions lie in the small  $2\%$  bandwidth around  $13.5\text{ nm}$  that is so relevant for plasma light sources for state-of-the-art nanolithography. Furthermore, we provide state-of-the-art *ab initio* calculations of  $\text{Sn}^{15+}$  using the configuration-interaction many-body perturbation code AMBiT and find it to be in excellent agreement with the experimental data at a  $0.3\%$  average deviation. These AMBiT calculations outperform other theory work by almost an order of magnitude.

## ACKNOWLEDGMENTS

Part of this work was carried out at the Advanced Research Center for Nanolithography, a public-private partnership between the University of Amsterdam, the Vrije Universiteit Amsterdam, the Netherlands Organization for Scientific Research (NWO), and the semiconductor equipment manufacturer ASML. This project has received funding from European Research Council (ERC) Starting Grant No. 802648 and is part of the VIDI research program with Project No. 15697, which is financed by NWO. J.S. and O.O.V. thank the MPIK in Heidelberg for the hospitality during the measurement campaign.

- 
- [1] F. Torretti, J. Sheil, R. Schupp, M. M. Basko, M. Bayraktar, R. A. Meijer, S. Witte, W. Ubachs, R. Hoekstra, O. O. Versolato, A. J. Neukirch, and J. Colgan, *Nat. Commun.* **11**, 2334 (2020).
  - [2] O. O. Versolato, *Plasma Sources Sci. Technol.* **28**, 083001 (2019).
  - [3] G. O’Sullivan, B. Li, R. D’Arcy, P. Dunne, P. Hayden, D. Kilbane, T. McCormack, H. Ohashi, F. O’Reilly, P. Sheridan, E. Sokell, C. Suzuki, and T. Higashiguchi, *J. Phys. B* **48**, 144025 (2015).
  - [4] J. Benschop, V. Banine, S. Lok, and E. Loopstra, *J. Vac. Sci. Technol. B* **26**, 2204 (2008).
  - [5] V. Y. Banine, K. N. Koshelev, and G. H. P. M. Swinkels, *J. Phys. D* **44**, 253001 (2011).
  - [6] S. S. Churilov and A. N. Ryabtsev, *Opt. Spectrosc.* **101**, 169 (2006).
  - [7] A. N. Ryabtsev, É. Y. Kononov, and S. S. Churilov, *Opt. Spectrosc.* **105**, 844 (2008).
  - [8] S. S. Churilov and A. N. Ryabtsev, *Opt. Spectrosc.* **100**, 660 (2006).
  - [9] S. S. Churilov and A. N. Ryabtsev, *Phys. Scr.* **73**, 614 (2006).
  - [10] R. D’Arcy, H. Ohashi, S. Suda, H. Tanuma, S. Fujioka, H. Nishimura, K. Nishihara, C. Suzuki, T. Kato, F. Koike, J. White, and G. O’Sullivan, *Phys. Rev. A* **79**, 042509 (2009).
  - [11] H. Ohashi, S. Suda, H. Tanuma, S. Fujioka, H. Nishimura, K. Nishihara, T. Kai, A. Sasaki, H. A. Sakaue, N. Nakamura, and S. Ohtani, *J. Phys.: Conf. Ser.* **163**, 012071 (2009).
  - [12] H. Ohashi, S. Suda, H. Tanuma, S. Fujioka, H. Nishimura, A. Sasaki, and K. Nishihara, *J. Phys. B* **43**, 065204 (2010).
  - [13] C. Suzuki, T. Kato, H. A. Sakaue, D. Kato, K. Sato, N. Tamura, S. Sudo, N. Yamamoto, H. Tanuma, H. Ohashi, R. D’Arcy, and G. O’Sullivan, *J. Phys. B* **43**, 074027 (2010).
  - [14] C. Suzuki, T. Kato, H. A. Sakaue, D. Kato, I. Murakami, K. Sato, N. Tamura, S. Sudo, N. Yamamoto, H. Tanuma, H. Ohashi, R. D’Arcy, C. S. Harte, and G. O’Sullivan, *AIP Conf. Proc.* **1344**, 21 (2011).

- [15] F. Torretti, A. Windberger, A. Ryabtsev, S. Dobrodey, H. Bekker, W. Ubachs, R. Hoekstra, E. V. Kahl, J. C. Berengut, J. R. Crespo López-Urrutia, and O. O. Versolato, *Phys. Rev. A* **95**, 042503 (2017).
- [16] A. Windberger, F. Torretti, A. Borschevsky, A. Ryabtsev, S. Dobrodey, H. Bekker, E. Eliav, U. Kaldor, W. Ubachs, R. Hoekstra, J. R. Crespo López-Urrutia, and O. O. Versolato, *Phys. Rev. A* **94**, 012506 (2016).
- [17] F. Torretti, R. Schupp, D. Kurilovich, A. Bayerle, J. Scheers, W. Ubachs, R. Hoekstra, and O. O. Versolato, *J. Phys. B* **51**, 045005 (2018).
- [18] R. Schupp, F. Torretti, R. A. Meijer, M. Bayraktar, J. Scheers, D. Kurilovich, A. Bayerle, K. S. E. Eikema, S. Witte, W. Ubachs, R. Hoekstra, and O. O. Versolato, *Phys. Rev. Appl.* **12**, 014010 (2019).
- [19] C. Biedermann, R. Radtke, R. Seidel, and T. Pütterich, *Phys. Scr.* **2009**, 014026 (2009).
- [20] J. Yatsurugi, E. Watanabe, H. Ohashi, H. A. Sakaue, and N. Nakamura, *Phys. Scr.* **2011**, 014031 (2011).
- [21] S. Ali and N. Nakamura, *J. Quant. Spectrosc. Radiat. Transf.* **198**, 112 (2017).
- [22] K. Fahy, E. Sokell, G. O'Sullivan, A. Aguilar, J. M. Pomeroy, J. N. Tan, and J. D. Gillaspay, *Phys. Rev. A* **75**, 032520 (2007).
- [23] J. Reader, J. D. Gillaspay, D. Osin, and Y. Ralchenko, *J. Phys. B* **47**, 145003 (2014).
- [24] W. Li, Z. Shi, Y. Yang, J. Xiao, T. Brage, R. Hutton, and Y. Zou, *Phys. Rev. A* **91**, 062501 (2015).
- [25] E. Träbert, P. Beiersdorfer, N. S. Brickhouse, and L. Golub, *Astron. Astrophys.* **586**, A115 (2016).
- [26] J. K. Lepson, P. Beiersdorfer, G. V. Brown, S. M. Kahn, D. A. Liedahl, C. W. Mauche, and S. B. Utter, *Rev. Mex. Astron. Astrophys.* **9**, 137 (2000).
- [27] J. K. Lepson, P. Beiersdorfer, G. V. Brown, D. A. Liedahl, S. B. Utter, N. S. Brickhouse, A. K. Dupree, J. S. Kaastra, R. Mewe, and S. M. Kahn, *Astrophys. J.* **578**, 648 (2002).
- [28] J. K. Lepson, P. Beiersdorfer, E. Behar, and S. M. Kahn, *Nucl. Instrum. Methods Phys. Res. B* **235**, 131 (2005).
- [29] I. E. Golovkin, R. C. Mancini, S. J. Louis, R. W. Lee, and L. Klein, *J. Quant. Spectrosc. Radiat. Transf.* **75**, 625 (2002).
- [30] R. D. Cowan, *The Theory of Atomic Structure and Spectra*, modified by A. Kramida (University of California Press, Berkeley, 1981).
- [31] M. F. Gu, *Can. J. Phys.* **86**, 675 (2008).
- [32] K. M. Aggarwal and F. P. Keenan, *At. Data Nucl. Data Tables* **107**, 221 (2016).
- [33] E. V. Kahl and J. C. Berengut, *Comput. Phys. Commun.* **238**, 232 (2019).
- [34] S. W. Epp, J. R. Crespo López-Urrutia, M. C. Simon, T. Baumann, G. Brenner, R. Ginzler, N. Guerassimova, V. Mäckel, P. H. Mokler, B. L. Schmitt, H. Tawara, and J. Ullrich, *J. Phys. B* **43**, 194008 (2010).
- [35] T. Harada and T. Kita, *Appl. Opt.* **19**, 3987 (1980).
- [36] A. Kramida, Yu. Ralchenko, J. Reader, and NIST ASD Team, NIST Atomic Spectra Database, Ver. 5.7.1 (National Institute of Standards and Technology, Gaithersburg, MD, 2019), <http://physics.nist.gov/asd>.
- [37] J. Sugar, W. L. Rowan, and V. Kaufman, *J. Opt. Soc. Am. B* **8**, 2026 (1991).
- [38] J. Sugar, W. L. Rowan, and V. Kaufman, *J. Opt. Soc. Am. B* **9**, 1959 (1992).
- [39] H. Bekker, O. O. Versolato, A. Windberger, N. S. Oreshkina, R. Schupp, T. M. Baumann, Z. Harman, C. H. Keitel, P. O. Schmidt, J. Ullrich, and J. R. Crespo López-Urrutia, *J. Phys. B* **48**, 144018 (2015).
- [40] Q. Lu, J. He, H. Tian, M. Li, Y. Yang, K. Yao, C. Chen, J. Xiao, J. G. Li, B. Tu, and Y. Zou, *Phys. Rev. A* **99**, 042510 (2019).
- [41] G. C. Rodrigues, P. Indelicato, J. P. Santos, P. Patté, and F. Parente, *At. Data Nucl. Data Tables* **86**, 117 (2004).
- [42] M. S. Gockenbach, *Finite-Dimensional Linear Algebra* (CRC Press, 2010), p. 361.
- [43] M. W. Berry, M. Browne, A. N. Langville, V. P. Pauca, and R. J. Plemmons, *Comput. Stat. Data Anal.* **52**, 155 (2007).
- [44] A. Kramida, A suite of atomic structure codes originally developed by R. D. Cowan adapted for Windows-based personal computers (National Institute of Standards and Technology, 2018), *NIST Public DATA Repository*, doi:10.18434/T4/1502500 (Accessed 2020-06-05).
- [45] C. Shah, P. Amaro, R. Steinbrügge, C. Beilmann, S. Bernitt, S. Fritzsche, A. Surzhykov, J. R. C. López-Urrutia, and S. Tashenov, *Phys. Rev. E* **93**, 061201(R) (2016).
- [46] C. Shah, H. Jörg, S. Bernitt, S. Dobrodey, R. Steinbrügge, C. Beilmann, P. Amaro, Z. Hu, S. Weber, S. Fritzsche, A. Surzhykov, J. R. Crespo López-Urrutia, and S. Tashenov, *Phys. Rev. A* **92**, 042702 (2015).
- [47] R. D'Arcy, H. Ohashi, S. Suda, H. Tanuma, S. Fujioka, H. Nishimura, K. Nishihara, C. Suzuki, T. Kato, F. Koike, A. O'Connor, and G. O'Sullivan, *J. Phys. B* **42**, 165207 (2009).
- [48] J. O. Ekberg, J. E. Hansen, and J. Reader, *J. Opt. Soc. Am.* **62**, 1143 (1972).
- [49] L. J. Curtis and P. S. Ramanujam, *Phys. Scr.* **27**, 417 (1983).
- [50] L. J. Curtis, *Phys. Rev. A* **35**, 2089 (1987).
- [51] M. Even-Zohar and B. S. Fraenkel, *J. Phys. B* **5**, 1596 (1972).
- [52] G. O'Sullivan, J. T. Costello, and P. K. Carroll, *J. Phys. B* **17**, 345 (1984).
- [53] J. T. Costello and G. O'Sullivan, *J. Phys. B* **17**, 4477 (1984).
- [54] J. Reader, *Atoms* **4**, 31 (2016).
- [55] J. Reader and M. D. Lindsay, *Phys. Scr.* **91**, 025401 (2016).
- [56] J. O. Ekberg, J. E. Hansen, and J. Reader, *J. Opt. Soc. Am.* **62**, 1139 (1972).
- [57] A. Goyal, I. Khatri, S. Aggarwal, A. K. Singh, and M. Mohan, *Can. J. Phys.* **93**, 487 (2014).
- [58] V. A. Dzuba, V. V. Flambaum, and M. G. Kozlov, *Phys. Rev. A* **54**, 3948 (1996).
- [59] J. C. Berengut, V. V. Flambaum, and M. G. Kozlov, *Phys. Rev. A* **73**, 012504 (2006).
- [60] J. C. Berengut, *Phys. Rev. A* **94**, 012502 (2016).
- [61] V. V. Flambaum and J. S. M. Ginges, *Phys. Rev. A* **72**, 052115 (2005).
- [62] J. S. M. Ginges and J. C. Berengut, *J. Phys. B* **49**, 095001 (2016).
- [63] J. S. M. Ginges and J. C. Berengut, *Phys. Rev. A* **93**, 052509 (2016).
- [64] A. J. Geddes, D. A. Czapski, E. V. Kahl, and J. C. Berengut, *Phys. Rev. A* **98**, 042508 (2018).